Chemical Engineering Journal 151 (2009) 66–72

Contents lists available at ScienceDirect

Chemical Engineering Journal

journal homepage: www.elsevier.com/locate/cej

Electrochemical synthesis of Fe_xNi_{1-x} nanostructures for environmental remediation

Yongsuk Hong, Youngwoo Rheem, Min Lai, David M. Cwiertny, Sharon L. Walker**, Nosang V. Myung*

Department of Chemical & Environmental Engineering, University of California, Riverside, Riverside, CA 92521, United States

ARTICLE INFO

Article history:
Received 30 July 2008
Received in revised form 26 January 2009
Accepted 29 January 2009

Keywords:
Nanoparticles
Electrodeposition
FeNi alloy
Environmental remediation
Chlorinated ethane

ABSTRACT

Fe_xNi_{1-x} nanostructures with different compositions ($0 < x < 1.0$) were electrodeposited from simple aqueous electrolytes with different ferric ion and nickel ion ratios. Composition, morphology, crystal structure, magnetic properties and electronegativity of the synthesized Fe_xNi_{1-x} nanostructures were systematically investigated. As the composition of Fe (x) in Fe_xNi_{1-x} nanostructures decreased from 1.0 to 0, the morphology changed from dendritic to nanoparticles and thin plates. The X-ray diffraction (XRD) patterns revealed that the dominant crystal structures shifted from metallic body centered cubic (bcc) for iron-rich Fe_xNi_{1-x} to mixed bcc and faced center cubic (fcc) for near equiatomic FeNi to rhombohedral/hexagonal for nickel-rich FeNi. The magnetic saturation and isoelectric point were also strongly dependent on nanostructure composition. Specifically, the magnetic saturation decreased and the isoelectric point increased with decreasing Fe content. When Fe content in Fe_xNi_{1-x} nanostructures was greater than 0.5 ($x > 0.5$), Fe_xNi_{1-x} nanostructures showed mainly metallic (zero-valent) Fe present as determined by XRD and selected area electron diffraction (SAED) patterns. Accordingly, $Fe_{1.0}$, $Fe_{0.71}Ni_{0.29}$ and $Fe_{0.55}Ni_{0.45}$ exhibited reactivity toward 1,1,1,2-tetrachloroethane, with $Fe_{1.0}$ yielding the greatest rate of reductive dechlorination.

1. Introduction and background

Nanostructured materials having a large surface-to-volume ratio possess very different properties from their bulk counterparts and are of great interest due to their many potential applications [1–4]. Magnetic nanostructures such as iron oxide nanoparticles (i.e., magnetite (Fe_3O_4) and maghemite (γ-Fe_2O_3)) are widely used in ferrofluids for audio speakers [5], magnetic resonance imaging [6,7], magnetic storage media [8], and site-specific gene and drug delivery [9,10]. Fe_xNi_{1-x} alloys with different compositions have been also used in many industrial fields due to their diversity in magnetic properties. Permalloy (20% iron, 80% nickel), for example, has been used in magnetic recording heads [11,12] and invar (64% iron, 36% nickel) has applications in precision instruments such as shadow masks for color televisions [13]. Nickel hydroxide, on the other hand, is the main active material for cathodes in alkaline rechargeable batteries [14–16].

Extensive efforts to synthesize iron oxide and Fe_xNi_{1-x} nanostructures have been devoted not only to the above applications, but also to the development of materials for environmental remediation [2,17–23]. Nanoscale iron oxides such as magnetite and maghemite have been used as adsorbents to remove arsenic from water [2,17]. Nanoscale zero-valent Fe, Pd/Fe, and Ni/Fe particles have also been studied and synthesized for environmental remediation of toxic compounds including chlorinated compounds, organic dyes, and heavy metals [18–23]. The bimetallic nanoparticles, such as Pd/Fe and Ni/Fe particles, have been observed to have around 1–3 orders of magnitude higher rate of chlorinated hydrocarbon degradation relative to microscale commercial Fe particles, due to their higher surface area-to-volume ratio and the catalytic nature of the metal additives to Fe [19,21].

Various wet chemical methods have been employed to synthesize nanoscale iron oxides, nickel oxides, metallic Fe, metallic Ni, and bimetallic Ni/Fe particles [24]. For the synthesis of nanoscale iron oxides, chemical precipitation [25,26], hydrothermal [27], thermolysis [28,29], and electrodeposition [2,30] were successfully used. However, nanoscale metallic Fe (zero-valent iron) previously used for environmental remediation have mostly been synthesized by the chemical reduction method from ferric or ferrous solutions in the presence of sodium borohydride with subsequent galvanic displacement of less noble metallic iron nanoparticles with more noble metals (e.g., Ni, Pd) to generate bimetallic nanoparticles (e.g., Ni/Fe and Pd/Fe) [18–23].

Compared to other wet chemical methods, electrodeposition is simple, fast, inexpensive, and manufacturable and can be an

* Corresponding author. Tel.: +1 951 827 7710; fax: +1 951 827 5696.
** Corresponding author. Tel.: +1 951 827 6094; fax: +1 951 827 5696.
E-mail addresses: swalker@engr.ucr.edu (S.L. Walker), myung@engr.ucr.edu (N.V. Myung).

1385-8947/$ – see front matter © 2009 Elsevier B.V. All rights reserved.
doi:10.1016/j.cej.2009.01.048

excellent alternative method of synthesizing nanoscale materials, such as nanowires [31–33], nanotubes [34], and nanoparticles [2,30]. In our prior work, it was demonstrated that the particle size, shape, and production rate of crystalline maghemite (γ-Fe_2O_3) nanoparticles were effectively controlled by adjusting the electrodeposition conditions [2]. Additionally, monodisperse crystalline zero-valent iron, FeNi, and FePd nanowires could be synthesized using template-directed electrodeposition method [33].

In this work, Fe_xNi_{1-x} nanostructures were electrodeposited as a function of Fe^{3+} and Ni^{2+} concentration in solution to investigate the capacity of this method to generate reactive Fe_xNi_{1-x} alloy nanostructures with controlled composition. Hence, the composition, morphology, crystal structure, magnetic properties, and electronegativity of electrochemically synthesized Fe_xNi_{1-x} nanostructures were measured, and the potential of these Fe_xNi_{1-x} nanostructures for environmental remediation of a model chlorinated hydrocarbon was examined.

2. Materials and methods

2.1. Chemicals

Chemicals used in this study were $FeCl_3$ (Fisher, ACS reagent grade), $NiCl_2{\cdot}6H_2O$ (Fisher, ACS reagent grade), 1,1,1,2-Tetrachloroethane (1,1,1,2-TeCA, 99%, Aldrich), and hexane (99%, Aldrich). The buffer solution of 25 mM Tris (tris(hydroxymethyl)-aminomethane, 99%, Sigma) in 0.1 M NaCl (99%, Sigma–Aldrich) used for reactivity studies was prepared using deionized water (Milli-Q Plus UV, Millipore) and was deoxygenated by purging with high purity N_2 gas (99.99%) for more than one and half hours.

2.2. Electrochemical synthesis and characterization

Fe_xNi_{1-x} nanostructures were electrochemically synthesized from six different electrolytes by varying the iron/nickel ion ratios in solution which is at a fixed total metal ions concentration of 0.01 M. The solution chemistry was varied according to $[Fe^{3+}]/([Fe^{3+}]+[Ni^{2+}])$ ratios: 0, 0.1, 0.25, 0.5, 0.75, and 1.0, which is shown in Table 1. The pH of the solution was adjusted to 2.0 with HCl or NaOH. A 100 mL glass jar with water jacket at 20 °C was used with a working volume of 50 mL. Steel (Kocour, Chicago, IL) and platinum-coated titanium (Technic Inc., Anaheim, CA) sheets were used as cathode and anode, respectively. The surface area of both electrodes was fixed at 4 cm^2. Electrodeposition of Fe_xNi_{1-x} nanostructures was conducted in galvanostatic mode with a fixed current density of 1 A/cm^2 using a power supply (Hewlett-Packard, 6655A, Houston, TX). The deposition time was fixed at 2 min. As the deposition was initiated, the potential began from approximately 80 V and gradually decreased to 50 V. The resulting nanostructures were washed three times with ultrapure water by centrifugation at 10,000 × *g* for 10 min and then vacuum-dried at 60 °C overnight. Dried samples were immediately used for the characterization. For reactivity test, dried samples were stored in an anaerobic chamber until used.

The composition of nanostructures was determined using an atomic absorption spectrometer (AAnalyst 800, PerkinElmer, Waltham, MA). The morphology of Fe_xNi_{1-x} was characterized by transmission electron microscopy (TEM) in a FEI-PHILIPS CM300 electron microscope (Hillsboro, OR) operated at 200 kV. The samples were prepared by placing a drop of a diluted suspension of each sample in ultrapure water onto a carbon coated copper grid and allowing water to evaporate at room temperature.

The crystalline structure of Fe_xNi_{1-x} was determined by X-ray diffraction using a D8 Advanced diffractometer (Bruker, Madison, WI) with Cu Kα radiation (λ = 0.154 nm). The surface area was measured by Brunauer–Emmett–Teller (BET) N_2 method (ASAP 2010, Micromeritics, Norcross, GA). Electrophoretic mobility was measured using a ZetaPALS (Brookhaven Instruments Corporation, Holtsville, NY) to get the isoeletric point (IEP), which was conducted at ionic strength of 1 mM KCl (Fisher, ACS reagent grade) from approximately pH 4 to 12. The magnetic properties, such as magnetic saturation (M_S) and coercivity (H_C), were measured using a vibrating sample magnetometer (VSM, ADE Tech, Model 1660, Westwood, MA) at room temperature with applied magnetic field up to ±10 kOe.

Table 1
Solution chemistry used for electrodeposition.

$[Fe^{3+}]/[Fe^{3+}]+[Ni^{2+}]$	Fe^{3+}, M	Ni^{2+}, M
1.0	0.01	0
0.75	0.75	0.25
0.5	0.5	0.5
0.25	0.25	0.75
0.1	0.1	0.9
0	0	0.01

2.3. Reactivity experiments

Reactivity experiments were conducted with three types of the Fe_xNi_{1-x} nanostructures to explore their capacity to reduce a model chlorinated solvent. All reactivity tests were carried out in vials (20 mL, nominal volume) that were free of headspace and sealed with Teflon-faced butyl rubber septa (Wheaton, Millville, NJ). Within an anaerobic chamber, synthesized Fe_xNi_{1-x} nanostructures were weighed into vials that were then filled with deoxygenated buffer solution. Each vial contained 0.1 M NaCl/25 mM Tris buffer (pH 7.0) and a Fe_xNi_{1-x} nanostructure loading of 1.0 g/L. After assembly, vials were removed from the anaerobic chamber and reactivity experiments were conducted immediately. To initiate the reaction, 36 μL of a solution of 55.56 mM 1,1,1,2-tetrachloroethane (1,1,1,2-TeCA) in methanol was added to the sealed vial via a 100 μL syringe, resulting in a final concentration of 100 μM (16.8 mg/L). Control vials free of any Fe_xNi_{1-x} nanostructures were also conducted, and used to determine the initial concentration of 1,1,1,2-TeCA in the experimental reactors. The vials were mixed on a rotary shaker (Cole-Parmer, Model 7637-01) at 45 rpm at room temperature.

At each sampling time, 200 μL was removed from the reactor by simultaneously adding an equivalent volume of deoxygenated buffer so as to prevent the development of headspace over time. Aqueous samples were extracted using 2 mL of hexane, followed by subsequent dilutions in hexane. Diluted extracts were analyzed via a 7890A Gas Chromatograph (Agilent Tech., Santo Clara, CA) with electron capture detection (ECD) and a RTX-1 column (30 m × 0.32 mm i.d. × 5 μm film thickness, Restek, Bellefonte, PA). Standards for these analyses were prepared in hexane and were analyzed in an identical manner to the experimental samples.

3. Results and discussion

3.1. Electrochemical synthesis and characterization

As electrodeposition was initiated, gas evolution occurred at both electrodes and powdered black deposits were formed on the cathode. After a reaction time of 2 min, solution pH remained nearly constant at pH 2.0 ± 0.1. Hydrogen gas bubbled up at the steel cathode, while oxygen gas was produced at the platinum coated titanium anode, resulting in constant solution pH during the electrodeposition. The dependence of resulting deposited Fe content on the ratios of $[Fe^{3+}]$ to $([Fe^{3+}]+[Ni^{2+}])$ in electrolytes is presented in Fig. 1. Since the atomic absorption spectrometer can not detect oxygen (O) and hydrogen (H) content in Fe_xNi_{1-x}, the Fe content at

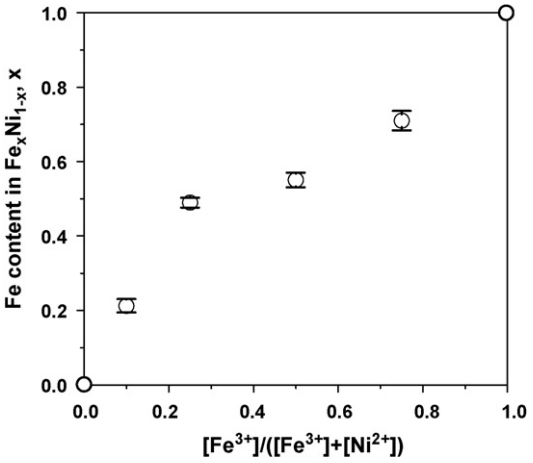

Fig. 1. Dependence of Fe content on the ratio of $[Fe^{3+}]/([Fe^{3+}]+[Ni^{2+}])$. Error bars represent ± one standard deviation from a minimum of five samples.

Y axis represents the atomic % ratio of Fe to (Fe + Ni) in Fe_xNi_{1-x}. Deposited Fe content increased from 0 to 0.21, 0.49, 0.55, 0.71, and 1.0 atomic fraction, as the ratio of $[Fe^{3+}]$ to $([Fe^{3+}]+[Ni^{2+}])$ in electrolytes varied from 0 to 0.1, 0.25, 0.5, 0.75, and 1.0, respectively. The Fe content in deposits was greater than in solution when the ratio of $[Fe^{3+}]$ to $([Fe^{3+}]+[Ni^{2+}])$ in electrolytes was less than 0.75. The electrodeposition of Fe-Ni is known to exhibit an anomalous co-deposition in which there is preferential deposition of the less noble Fe [35], although there is not an accepted theory to explain this phenomenon.

Fig. 2 presents TEM images of synthesized Fe_xNi_{1-x} nanostructures. It can be seen that the morphology and size of the Fe_xNi_{1-x} were greatly influenced by electrolyte composition. For Fe contents greater than 50% (i.e., $x > 0.5$), dendritic structures were observed with approximately 30–120 nm thick branches (Fig. 2a–c). It should be noted that spherical nanoparticles of approximately 5–30 nm in diameter were also observed between the branches of the dendrites, and that these spherical nanoparticles were more prevalent in $Fe_{0.71}Ni_{0.29}$ and $Fe_{0.55}Ni_{0.45}$ nanostructures than with $Fe_{1.0}$. For deposited Fe contents less than 50% ($x < 0.5$), the dendritic shape

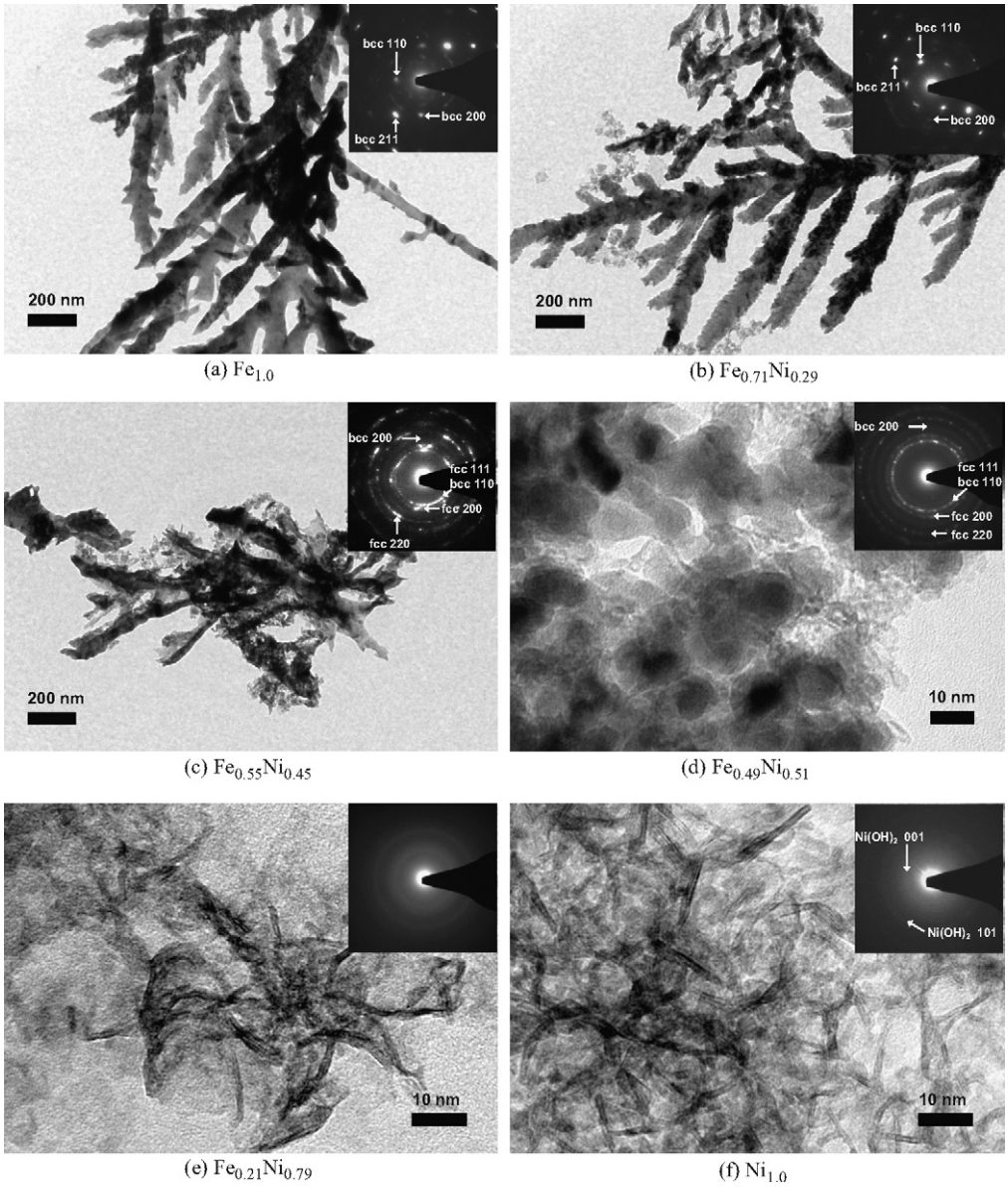

Fig. 2. TEM images of Fe_xNi_{1-x} nanostructures. Insets show the selected area electron diffraction (SAED) patterns.

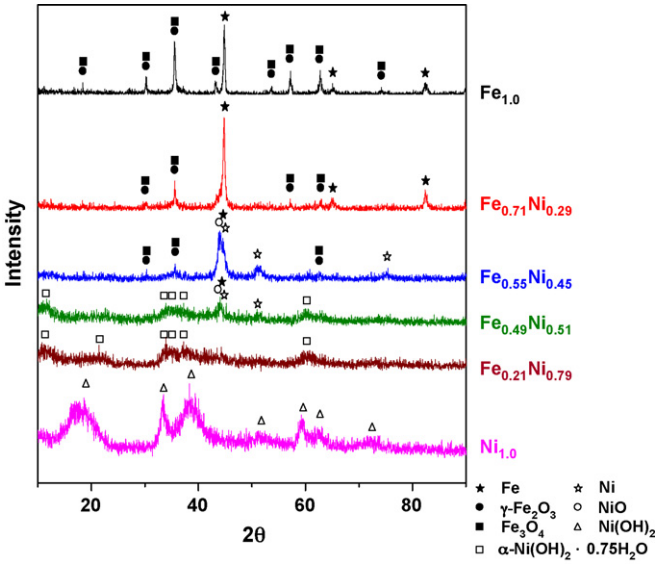

Fig. 3. X-ray diffraction patterns of Fe_xNi_{1-x} nanostructures synthesized from solutions with different ratios of Fe^{3+} and Ni^{2+}.

disappeared and the morphology changed (Fig. 2d–f). Notably, for $Fe_{0.49}Ni_{0.51}$, 5–30 nm in diameter nanoparticles were dominant and a few thin plates were also observed, while the majority of structures for Fe_xNi_{1-x} with Ni content greater than 0.79 were thin plates.

The inset in Fig. 2 shows the selected area electron diffraction (SAED) patterns. X-ray diffraction (XRD) patterns of Fe_xNi_{1-x} nanostructures are shown in Fig. 3. It reveals that the crystal structures and crystallinity changed as a function of the composition. For example, the main diffraction peaks (2θ of 44.7°, 65.2°, and 82.3°) of iron-rich Fe_xNi_{1-x} nanostructures ($x \geq 0.71$) indicate that they consist of randomly oriented polycrystalline nanostructures with body centered cubic (bcc) structures. Minor diffraction peaks were identified to be magnetite (Fe_3O_4) or maghemite (γ-Fe_2O_3). Since the Fe_xNi_{1-x} nanostructures in this study were electrochemically synthesized open to the air and then washed three times with deionized water containing natural dissolved oxygen, washing and drying steps likely induced the formation of iron oxides at the surface. For nearly equiatomic FeNi (i.e., $Fe_{0.55}Ni_{0.45}$ and $Fe_{0.49}Ni_{0.51}$) nanoparticles, randomly oriented polycrystalline nanoparticles with mixed face centered cubic (fcc) and bcc structures were observed. The diffraction peaks at 2θ of 44.5°, 51.9°, and 76.4° corresponding to (1 1 1), (2 0 0), and (2 2 0) phases of fcc structures, respectively. On the other hand, the XRD patterns of nickel-rich Fe_xNi_{1-x} ($x \leq 0.21$) show very different crystal structure. The 2θ of $Fe_{0.21}Ni_{0.79}$ which showed rather poor crystalline phase is similar to the previously reported patterns of electrochemically deposited Fe-doped $Ni(OH)_2$ tubes [34] and is in accordance with the standard XRD patterns of α-$Ni(OH)_2 \cdot 0.75H_2O$ (JCPDS file No. 38-0715) which is rhombohedral structure. All the peaks for $Ni_{1.0}$ are in good agreement with the JCPDS file No. 14-0117, reflecting the sole existence of hexagonal structure of $Ni(OH)_2$.

Fig. 4a shows the average grain size of Fe_xNi_{1-x} nanostructures as a function of deposited Fe content. Average grain size was calculated from XRD patterns using the Scherrer's equation [36]. The average grain size of Fe was the largest, and grain size slowly decreased as the Fe content (x) of Fe_xNi_{1-x} nanostructures decreased from 1.0 to 0.55. Further, a more rapid drop in the average grain size occurred with decreasing Fe content of Fe_xNi_{1-x} for $x < 0.49$. The broad peak widths of XRD patterns as seen in Fig. 3 for $Fe_{0.49}Ni_{0.51}$, $Fe_{0.21}Ni_{0.79}$, and $Ni_{1.0}$ indicate that the crystalline sizes are very small and the average grain size of those nanostructures are 2.4, 2.8, and 5.6 nm,

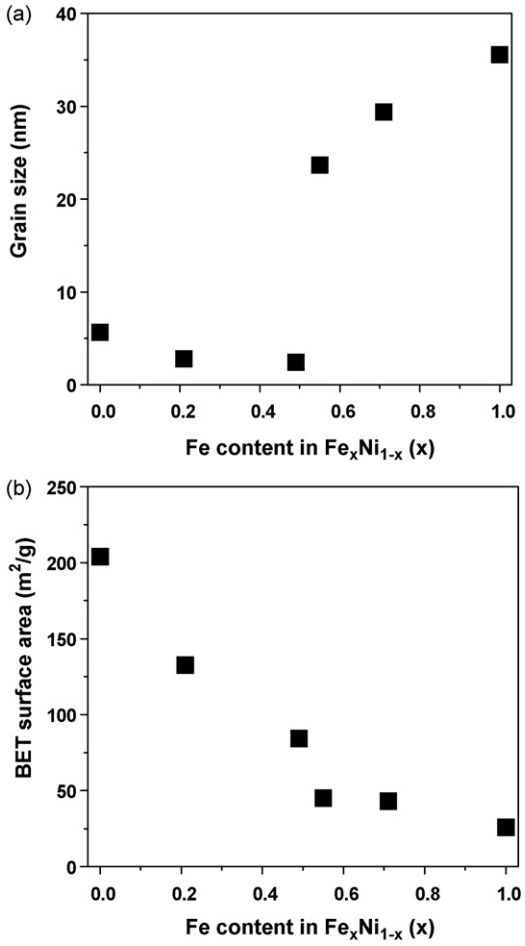

Fig. 4. (a) Average grain size and (b) BET surface area of Fe_xNi_{1-x} nanostructures as a function of Fe content in deposit.

respectively. Fig. 4b shows that BET surface area increased with increasing Ni content in Fe_xNi_{1-x} nanostructures. The BET surface areas of $Fe_{1.0}$, $Fe_{0.71}Ni_{0.29}$ and $Fe_{0.55}Ni_{0.45}$ nanostructures having dendritic shape were 25.9, 43.0, and 45.2 m^2/g, respectively. As seen in Fig. 2, it is believed that the spherical nanoparticles observed for $Fe_{0.71}Ni_{0.29}$ and $Fe_{0.55}Ni_{0.45}$ nanostructures resulted in their higher BET surface area as compared to $Fe_{1.0}$. It can be readily seen in Fig. 4 that the BET surface area of Fe_xNi_{1-x} nanostructures increased as the grain size of those nanostructures decreased.

Fig. 5a shows the Hysteresis curve of Fe_xNi_{1-x} nanostructures at room temperature, and Fig. 5b and c represents the magnetic saturation (M_S) and coercivity (H_C) of Fe_xNi_{1-x} nanostructures, respectively. Results show that magnetic properties of both M_S and H_C were dependent on the composition of Fe_xNi_{1-x} nanostructures. M_S and H_C of Fe_xNi_{1-x} with $x > 0.5$ are relatively much higher than those of Fe_xNi_{1-x} with $x < 0.5$ and there was the transition zone where M_S and H_C rapidly decreased when Fe content was from 0.55 to 0.49. For example, M_S and H_C of $Fe_{0.55}Ni_{0.45}$ were 81 emu/g and 76 Oe, respectively, whereas those of $Fe_{0.49}Ni_{0.51}$ were 12.4 emu/g and 2.0 Oe, respectively, indicating a transition from ferromagnetic to superparamagnetic state with no or almost no magnetic saturation and magnetic hysteresis. Results also show that $Ni_{1.0}$ nanostructures which are $Ni(OH)_2$ is paramagnetic [37].

The significant decrease in M_S with decreasing Fe content (x) below 0.5 may be mainly due to the change in the composition. The literature values of M_S for bulk iron (Fe), magnetite (Fe_3O_4), maghemite (γ-Fe_2O_3), and nickel (Ni) are 222, 92, 76, and 55 emu/g, respectively [38,39], suggesting that the more metallic Fe content

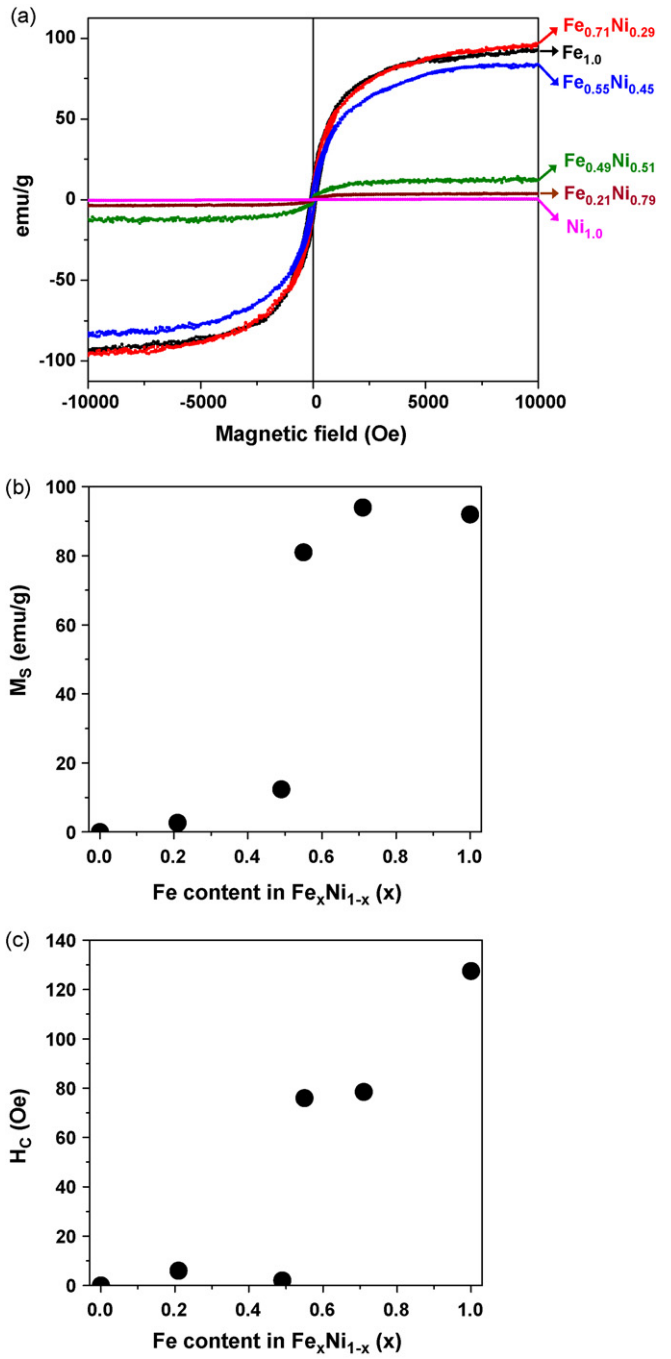

Fig. 5. (a) Hysteresis curves, (b) magnetic saturation and (c) coercivity of Fe_xNi_{1-x} nanostructures as a function of Fe content in deposit.

in the nanostructures, the greater the magnetic saturation (M_S). M_S of $Fe_{1.0}$, $Fe_{0.71}Ni_{0.29}$ and $Fe_{0.55}Ni_{0.45}$ that had mainly metallic Fe and iron oxides were 92, 94, and 81 emu/g, respectively, which were much greater than that of other Fe_xNi_{1-x} with $x < 0.5$ that contained paramagnetic $Ni(OH)_2$. Therefore, it is likely that the composition changes from the metallic Fe and iron oxides rich condition to the paramagnetic $Ni(OH)_2$ rich condition caused the rapid drop of M_S when $x < 0.5$. In addition, this rapid decrease in M_S might be also attributed to the decrease in size. It is known that M_S of a magnetic material in an external field is dependent upon the number of magnetic molecules in a single magnetic domain and is proportional to size of material [40]. It was also seen in this study (Fig. 4) that when Fe contents were less than 0.5, the surface area of the

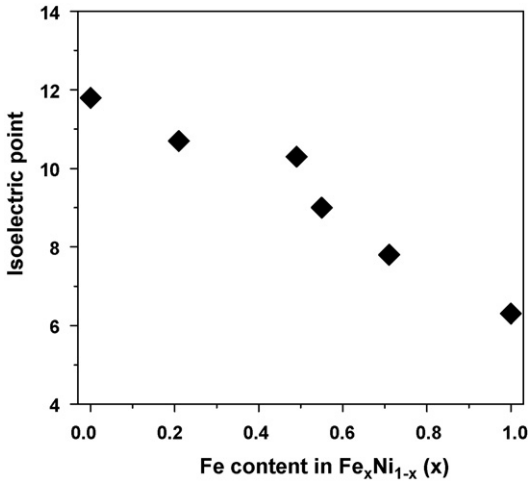

Fig. 6. Isoelectric point of Fe_xNi_{1-x} nanostructures as a function of Fe content in deposit.

Fe_xNi_{1-x} rapidly increased, indicating that the decrease in size (or the increase in surface area per unit mass) can be another reason for the rapid decrease in M_S.

Fig. 6 presents the isoelectric point (IEP) of $Fe_{1-x}Ni_x$ nanostructure as a function of Fe content. It was observed that the IEP of Fe_xNi_{1-x} nanostructures linearly increased as deposited Fe content decreased. For example, the $Ni_{1.0}$ nanostructure which is found to be entirely $Ni(OH)_2$ has an IEP of 11.8 while the $Fe_{1.0}$ nanostructure has IEP of 6.3. Other Fe_xNi_{1-x} nanostructures in this study showed intermediate IEP values between these two values varying as a function of deposited Fe contents. The IEP of metallic Fe (zero-valent iron) in the literature was reported to be 6.0 [41] and 8.2 [42], and that of $Ni(OH)_2$ was 11–12 [43]. While there have been a lack of IEP values for Fe_xNi_{1-x} nanostructures reported in the literature, comparable IEP values of γ-Fe_2O_3, Fe_3O_4, and NiO in the literatures are in the range of 6.7–7.5 [43–45], 5.9–8.0 [43,46–49], and 10.3 [43], respectively.

Results in this study indicated that IEP values of Fe_xNi_{1-x} were strongly influenced by the composition of Fe and Ni in deposits and increased with decreasing deposited Fe content, and these trends are supported by others reported in literature [41–49]. For remediation in the subsurface, the delivery of reactive nanoparticles to target compounds is essential. IEP data of Fe_xNi_{1-x} nanostructures may have an impact on their transport and stability in the aqueous environments. As aquifer materials generally are negatively charged under environmental pH, Fe_xNi_{1-x} nanostructures with higher Ni content would be less desirable for aquifer applications from an electrostatic standpoint; Fe_xNi_{1-x} nanostructures with higher Ni content are more positively charged and would be more attractive to aquifer materials.

3.2. Reactivity experiments

Batch experiments were conducted to investigate whether the electrochemically synthesized Fe_xNi_{1-x} nanostructures display reactivity toward a model organohalide, and thus could have future applications in environmental remediation. Zero-valent iron is an effective reductant toward a broad spectrum of pollutants including chlorinated solvents [21,23,50–52] and metallic Fe is known to be the primary source of reducing equivalents in bimetallic systems, as Ni alone is not reactive toward chlorinated solvents [53]. Hence, three Fe_xNi_{1-x} nanostructures with high Fe contents (i.e., $Fe_{1.0}$, $Fe_{0.71}Ni_{0.29}$ and $Fe_{0.55}Ni_{0.45}$) were selected by assuming that they also have the largest amount of reducing equivalents. The change in 1,1,1,2-TeCA concentration over time in systems

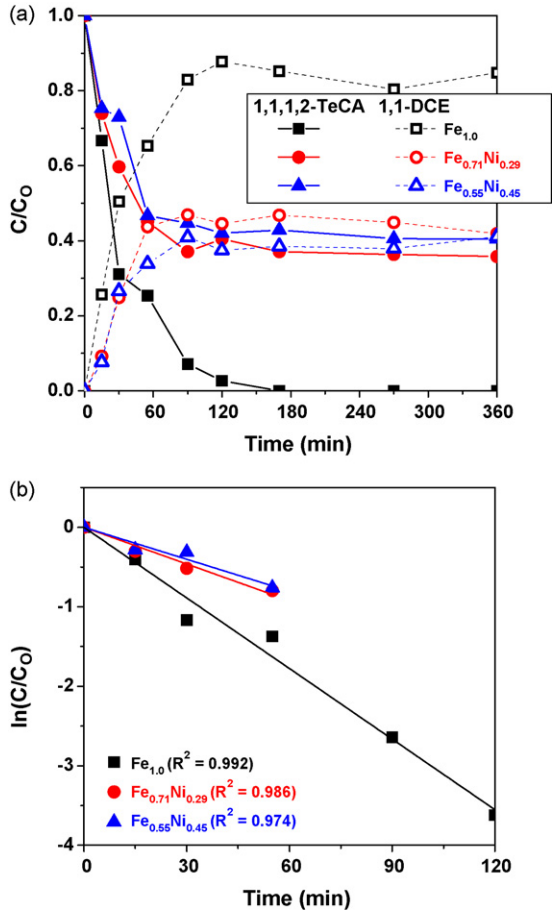

Fig. 7. (a) Reactivity result of Fe_xNi_{1-x} nanostructures with 1,1,1,2-TeCA. Solid and open symbols represent relative concentrations of 1,1,1,2-TeCA and 1,1-DCE, respectively. (b) Plots of pseudo-first-order reaction regression.

with each Fe_xNi_{1-x} nanostructure is presented in Fig. 7a. Complete reduction of 1,1,1,2-TeCA was observed with $Fe_{1.0}$ after 170 min of reaction time. In contrast, $Fe_{0.71}Ni_{0.29}$ and $Fe_{0.55}Ni_{0.45}$ reduced 60% of the initial 1,1,1,2-TeCA over 60–90 min, with no further loss being observed over the remainder of the experiment. As seen in Fig. 7a, 1,1-dichloroethylene (1,1-DCE) was the only reduction product detected for all Fe_xNi_{1-x} nanostructures examined in this study. These results are consistent with previous studies that have also reported reductive β-elimination as the dominant transformation pathway for 1,1,1,2-TeCA in zero-valent metal systems [54,55]. Carbon mass balances were roughly 85% in all experimental system. The slight loss of mass most likely results from minor products of 1,1-DCE reductive dehalogenation, such as ethane and ethylene, which were not quantified in this study.

Generally, the rate of pollutant transformation in zero-valent iron systems is pseudo-first-order [50,51,56–61] with respect to pollutant concentration (Eq. (1)).

$$-\frac{d[C]}{dt} = k_{SA} a_s \rho_m [C] = k_{obs}[C] \quad (1)$$

Applying Eq. (1) to the systems considered herein, [C] is the concentration of 1,1,1,2-TeCA ($mg\,L^{-1}$), k_{SA} is the surface-area-normalized rate constant ($L\,h^{-1}\,m^{-2}$), a_s is the specific surface area of Fe_xNi_{1-x} ($m^2\,g^{-1}$), ρ_m is the Fe_xNi_{1-x} mass concentration ($g\,L^{-1}$), and k_{obs} is the observed pseudo-first-order rate constant (per h). As shown in Fig. 7b, the concentration of 1,1,1,2-TeCA initially followed exponential decay in each reactor system, although deviations from this model consistent with surface passivation were observed for $Fe_{0.71}Ni_{0.29}$ and $Fe_{0.55}Ni_{0.45}$ nanostructures at greater timescales. Linear regression analysis performed over the time period shown in Fig. 7b were therefore used to determine the initial k_{obs} value for 1,1,1,2-TeCA reduction by $Fe_{1.0}$, $Fe_{0.71}Ni_{0.29}$ and $Fe_{0.55}Ni_{0.45}$. These values were determined to be 1.78, 0.92, and 0.80 h^{-1}, respectively, illustrating that the nanostructures consisting entirely of iron were most reactive.

In general, bimetallic zero-valent iron including Fe/Ni and Fe/Pd is more reactive toward organohalides relative to zero-valent iron [19,53,61–63]. For example, Fe/Ni nanoparticles were reported to be 50-fold more reactive toward trichloroethene (TCE) than Fe nanoparticles [19] and the reactivity of Fe/Pd nanoparticles toward tetrachloroethene (PCE) were two orders of magnitude greater than that of Fe nanoparticles [61]. It is proposed that bimetallic reductants are more reactive than metallic iron as a result of the additives' (e.g., Ni and Pd) superior ability to sorb atomic hydrogen generated via the reduction of water, and this atomic hydrogen is postulated to be the reactive entity responsible for degrading chlorinated hydrocarbons through a surface-mediated reaction [19,53,61,64]. However, in the current study, k_{obs} of $Fe_{1.0}$ demonstrates roughly 2-fold greater reactivity relative to $Fe_{0.71}Ni_{0.29}$ and $Fe_{0.55}Ni_{0.45}$ despite the surface area of $Fe_{1.0}$ being approximately 1.7 times lower than that of the other two. Accordingly, comparison of nanostructure reactivity on the basis of particle surface area reveals that $Fe_{1.0}$ ($k_{SA} = 6.86 \times 10^{-2}\,L\,m^{-2}\,h^{-1}$) is approximately 3–4 times more reactive toward 1,1,1,2-TeCA than $Fe_{0.71}Ni_{0.29}$ ($k_{SA} = 2.15 \times 10^{-2}\,L\,m^{-2}\,h^{-1}$) and $Fe_{0.55}Ni_{0.45}$ ($k_{SA} = 1.78 \times 10^{-2}\,L\,m^{-2}\,h^{-1}$), respectively. This unanticipated reactivity trend may be attributed to $Fe_{0.71}Ni_{0.29}$ and $Fe_{0.55}Ni_{0.45}$ being homogenous alloys rather than bimetallic heterogenous reductants generated from Ni coating on Fe surfaces. In homogenous alloys, the corrosion rate (i.e., reactivity) is strongly dependent on the composition of alloys where addition of nickel to iron monotonically increased the corrosion potentials and decreased corrosion rate with the lowest corrosion rate at near equiatomic FeNi [65].

The BET surface area for nanoscale (1–100 nm) zero-valent iron synthesized by wet chemical reduction method in the presence of borohydride in the literature is reported to be in the range of 28–59 m^2/g [19,22,55], which is in the similar range with three Fe_xNi_{1-x} nanostructures used in the current study (i.e., BET surface area of $Fe_{1.0}$, $Fe_{0.71}Ni_{0.29}$ and $Fe_{0.55}Ni_{0.45}$ were 25.9, 43.0, and 45.2 m^2/g, respectively). Compared to zero-valent iron materials used in other studies, the reactivity of $Fe_{1.0}$ is 8-fold lower than that of nanosized zero-valent iron particles ($k_{SA} = 5.4 \times 10^{-1}\,L\,m^{-2}\,h^{-1}$) which were synthesized by the borohydride reduction method [55]. However, the reactivity of $Fe_{1.0}$ is still 5-fold greater than that reported for microsize zero-valent iron ($k_{SA} = 1.4 \times 10^{-2}\,L\,m^{-2}\,h^{-1}$) which was the commercially available 100 mesh Fisher electrolytic iron [52].

4. Conclusions

Fe_xNi_{1-x} nanostructures were electrochemically synthesized from simple aqueous electrolyte. Composition, shape, crystal structure, magnetic properties and electronegativity of synthesized Fe_xNi_{1-x} nanostructures varied by the change in deposited Fe content. To our knowledge, this study first demonstrated that electrochemically synthesized Fe_xNi_{1-x} nanostructures have potential for environmental remediation for the reduction of chlorinated solvents and further studies are needed to expand the scope of the electrochemical synthesis method to fabricate zero-valent irons that have more reactivity.

Acknowledgements

The authors gratefully acknowledge the financial support from University of California Toxic Substances Research & Teaching Program (UC TSR & TP).

References

[1] A.P. Alivisatos, Synthesis of nanoparticles, Science 271 (1996) 933–937.
[2] H. Park, P. Ayals, M.A. Deshusses, A. Mulchandani, H. Choi, N.V. Myung, Electrodeposition of maghemite (γ-Fe_2O_3) nanoparticles, Chem. Eng. J. 139 (2007) 208–212.
[3] A.N. Shipway, E. Katz, I. Willner, Nanoparticle arrays on surfaces for electronic, optical, and sensor applications, Chemphyschem 1 (2000) 18–52.
[4] A.H. Latham, M.E. Williams, Controlling transport and chemical functionality of magnetic nanoparticles, Acc. Chem. Res. 41 (2008) 411–420.
[5] M.M. Miller, G.A. Prinz, S.F. Cheng, C. Bounnak, Detection of a micron-sized magnetic sphere using a ring-shaped anisotropic magnetoresistance-based sensor: a model for a magetoresistance-based biosensor, Appl. Phys. Lett. 81 (2002) 2211–2213.
[6] R.W. Briggs, Z. Wu, C.R.J. Mladinich, C. Stoupic, J. Gauger, T. Liebig, P.R. Ros, J.R. Ballinger, P. Kubilis, In vivo animal tests of an artifact-free contrast agent for gastrointestinal MRI, Magn. Reson. Imaging 15 (1997) 559–566.
[7] K.A. Hinds, J.M. Hill, E.M. Shapiro, M.O. Laukkanen, A.C. Silva, C.A. Combs, T.R. Varney, R.S. Balaban, A.P. Koretsky, C.E. Dunbar, Highly efficient endosomal labeling of progenitor and stem cells with large magnetic particles allows magnetic resonance imaging of single cells, Blood 102 (2003) 867–872.
[8] M.P. Sharrock, Particulate magnetic recording media: a review, IEEE Trans. Magn. 25 (1989) 4374–4389.
[9] S.R. Rudge, T.L. Kurtza, C.R. Vesselya, L.G. Catteralla, D.L. Williamson, Preparation, characterization, and performance of magnetic iron–carbon composite microparticles for chemotherapy, Biomaterials 21 (2000) 1411–1420.
[10] F. Scherer, M. Anton, U. Schillinger, J. Henke, C. Bergemann, A. Krüger, B. Gänsbacher, C. Plank, Magnetofection: enhancing and targeting gene delivery by magnetic force in vitro and in vivo, Gene Ther. 9 (2002) 102–109.
[11] P.C. Andricacos, L.T. Romankiw, Magnetically soft materials in data storage: their properties and electrochemistry, in: H. Gerischer, C.W. Tobias (Eds.), Advances in Electrochemical Science and Engineering, vol. 3, VCH, New York, 1994, pp. 227–321.
[12] N. Zech, E.J. Podlaha, D. Landolt, Rotating cylinder hull cell study of anomalous codeposition of binary iron-group alloys, J. Appl. Electrochem. 28 (1998) 1251–1260.
[13] M. Shiga, Invar alloys, Curr. Opin. Solid State Mater. Sci. 1 (1996) 340–348.
[14] S. Deabate, F. Fourgeot, F. Henn, X-ray diffraction and micro-Raman spectroscopy analysis of new nickel hydroxide obtained by electrodialysis, J. Power Sources 87 (2000) 125–136.
[15] R.S. Jayashree, P.V. Kamath, Factors governing the electrochemical synthesis of α-nickel (II) hydroxide, J. Appl. Electrochem. 29 (1999) 449–454.
[16] Q.-Z. Jiao, Z.-L. Tian, Y. Zhao, preparation of nickel hydroxide nanorods/nanotubes and microscopic nanorings under hydrothermal conditions, J. Nanopart. Res. 9 (2007) 519–522.
[17] C.T. Yavuz, J.T. Mayo, W.W. Yu, A. Prakash, J.C. Falkner, S. Yean, L. Cong, H.J. Shipley, A. Kan, M. Tomson, D. Natelson, V.L. Colvin, Low-field magnetic separation of monodisperse Fe_3O_4 nanocrystals, Science 314 (2006) 964–967.
[18] J. Feng, T.-T. Lim, Pathways and kinetics of carbon tetrachloride and chloroform reductions by nano-scale Fe and Fe/Ni particles: comparison with commercial micro-scale Fe and Zn, Chemosphere 59 (2005) 1267–1277.
[19] B. Schrick, J.L. Blough, A.D. Jones, T.E. Mallouk, Hydrodechlorination of trichloroethylene to hydrocarbons using bimetallic nickel-iron nanoparticles, Chem. Mater. 14 (2002) 5140–5147.
[20] W. Zhang, X. Quana, J. Wanga, Z. Zhangb, S. Chen, Rapid and complete dechlorination of PCP in aqueous solution using Ni–Fe nanoparticles under assistance of ultrasound, Chemosphere 65 (2006) 58–64.
[21] W.-X. Zhang, Nanoscale iron particles for environmental remediation: an overview, J. Nanopart. Res. 5 (2003) 323–332.
[22] C.-B. Wang, W.-X. Zhang, Synthesizing nanoscale iron particles for rapid and complete dechlorination of TCE and PCBs, Environ. Sci. Technol. 31 (1997) 2154–2156.
[23] A.D. Bokare, R.C. Chikate, C.V. Rode, K.M. Paknikar, Effect of surface chemistry of Fe-Ni nanoparticles on mechanistic pathways of azo dye degradation, Environ. Sci. Technol. 41 (2007) 7437–7443.
[24] M.A. Willard, L.K. Kurihara, E.E. Carpenter, S. Calvin, V.G. Harris, Chemically prepared magnetic nanoparticles, Int. Mater. Rev. 49 (2004) 125–170.
[25] T. Ishikawa, M. Kumagai, A. Yasukawa, K. Kandori, T. Nakayama, F. Yuse, Influences of metal ions on the formation of γ-FeOOH and magnetite rusts, Corros. Sci. 2002 (2002) 1073–1086.
[26] X.L. Xu, J.D. Guo, Y.Z. Wang, A novel technique by the citrate pyrolysis for preparation of iron oxide nanoparticles, Mater. Sci. Eng. 77 (2000) 207–209.
[27] D.-S. Bae, K.-S. Han, S.-B. Cho, S.-H. Choi, Synthesis of ultrafine Fe_3O_4 powder by glycothermal process, Mater. Lett. 37 (1998) 255–258.
[28] J. Rockenberger, E.C. Scher, A.P. Alivisatos, A new nonhydrolytic single-precursor approach to surfactant-capped nanocrystals of transition metal oxides, J. Am. Chem. Soc. 121 (1999) 11595–11596.
[29] T. Hyeon, S.S. Lee, J. Park, Y. Chung, H.B. Na, Synthesis of highly crystalline and monodisperse maghemite nanocrystallite without a size-selection process, J. Am. Chem. Soc. 123 (2001) 12798–12801.
[30] C. Pascal, J.L. Pascal, F. Favier, Electrochemical synthesis for the control of γ-Fe_2O_3 nanoparticle size. Morphology, microstructure, and magnetic behaviour, Chem. Mater. 11 (1999) 141–147.
[31] C.M. Hangarter, N.V. Myung, Magnetic alignment of nanowires, Chem. Mater. 17 (2005) 1320–1324.
[32] B.-Y. Yoo, Y. Rheem, W.P. Beyermann, N.V. Myung, Magnetically assembled 30 nm diameter nickel nanowire with ferromagnetic electrodes, Nanotechnology 17 (2007) 2512–2517.
[33] B.-Y. Yoo, S.C. Hernandez, B. Koo, Y. Rheem, N.V. Myung, Electrochemically fabricated zero-valent iron, iron-nickel, iron-palladium nanowires for environmental remediation application, Water Sci. Technol. 55 (2007) 149–156.
[34] S. Chou, F. Cheng, J. Chen, Electrochemical deposition of $Ni(OH)_2$ and Fe-doped $Ni(OH)_2$ tubes, Eur. J. Inorg. Chem. 2005 (2005) 4035–4039.
[35] A. Brenner, Electrodeposition of Alloys, Academic Press, New York, 1963.
[36] B.D. Culllity, S.R. Stock, Elements of X-ray Diffraction, 3rd ed., Prentice Hall, New Jersey, 2001.
[37] P. Xu, X.J. Han, X.H. Wang, C. Wang, H.T. Zhao, W.J. Zhang, Effect of $Ni(OH)_2$ coating on the electromagnetic properties of hexagonal barium ferrite, Mater. Chem. Phys. 108 (2008) 196–200.
[38] B.D. Culllity, Introduction to Magnetic Materials, Addison-Wesley, Reading, MA, 1972.
[39] J.H. Hwang, Magnetic properties of graphitically encapsulated nickel nanocrystals, J. Mater. Res. 12 (1997) 1076–1082.
[40] S.-H. Wu, D.-H. Chen, Synthesis and characterization of nickel nanoparticles by hydrazine reduction in ethylene glycol, J. Colloid Interface Sci. 259 (2003) 282–286.
[41] G.C.C. Yang, H.-C. Tu, C.-H. Hung, Stability of nanoiron slurries and their transport in the subsurface environment, Sep. Purif. Technol. 58 (2007) 166–172.
[42] Y.-P. Sun, X.-Q. Li, W.-X. Zhang, H.P. Wang, A method for the preparation of stable dispersion of zero-valent iron nanoparticles, Colloids Surf. A 308 (2007) 60–66.
[43] G.A. Parks, The isoelectric points of solid oxides, solid hydroxides, and aqueous hydorxo complex systems, Chem. Rev. 65 (1965) 177–198.
[44] M. Takfuji, S. Ide, H. Ihara, Z. Xu, Preparation of Poly(1-vinylimidazole)-grafted magnetic nanoparticles and their application for removal of metal ions, Chem. Mater. 16 (2004) 1977–1983.
[45] S. Yu, G.M. Chow, Carboxyl group ($-CO_2H$) functionalized ferrimagnetic iron oxide nanoparticles for potential bio-applications, J. Mater. Chem. 14 (2004) 2781–2786.
[46] G.D. Mendenhall, Y. Geng, J. Hwang, Optimization of long-term stability of magnetic fluids from magnetite and synthetic polyelectrolytes, J. Colloid Interface Sci. 184 (1996) 519–526.
[47] A.P. Philipse, M.P.B. van Bruggen, C. Pathmamanoharan, Magnetic silica dispersions: preparation and stability of surface-modified silica particles with a magnetic core, Langmuir 10 (1994) 92–99.
[48] S.A. Gomez-Lopera, R.C. Plaza, A.V. Delgado, Synthesis and characterization of spherical magnetite/biodegradable polymer composite particles, J. Colloid Interface Sci. 240 (2001) 40–47.
[49] E. Illes, E. Tombacz, The effect of humic acid adsorption on pH-dependent surface charging and aggregation of magnetite nanoparticles, J. Colloid Interface Sci. 295 (2006) 115–123.
[50] A. Agrawal, P.G. Tratnyek, Reduction of nitro aromatic compounds by zero-valent iron metal, Environ. Sci. Technol. 30 (1996) 153–160.
[51] M.J. Alowitz, M.M. Scherer, Kinetics of nitrate, nitrite and Cr(VI) reduction by iron metal, Environ. Sci. Technol. 36 (2002) 299–306.
[52] T.L. Johnson, M.M. Scherer, P.G. Tratnyek, Kinetics of halogenated organic compound degradation by iron metal, Environ. Sci. Technol. 30 (1996) 2634–2640.
[53] D.M. Cwiertny, S.J. Bransfield, A.L. Roberts, Influence of the oxidizing species on the reactivity of iron-based bimetallic reductants, Environ. Sci. Technol. 41 (2007) 3734–3740.
[54] W.A. Arnold, W.P. Ball, A.L. Roberts, Polychlorinated ethane reaction with zero-valent zinc: pathways and rate control, J. Contam. Hydrol. 40 (1999) 183–200.
[55] H. Song, E.R. Carraway, Reduction of chlorinated ethanes by nanosized zero-valent iron: kinetics, pathways, and effects of reaction conditions, Environ. Sci. Technol. 39 (2005) 6237–6245.
[56] L.T. Matheson, P.G. Tratnyek, Reductive dehalogenation of chlorinated methanes by iron metal, Environ. Sci. Technol. 28 (1994) 2045–2053.
[57] R.W. Gillham, S.F. O'Hannesin, Enhanced degradation of halogenated aliphatics by zero-valent iron, Ground Water 32 (1994) 958–967.
[58] V. Rajagopal, D.R. Burris, Reduction of 1,2-dibromoethane in the presence of zero-valent iron, Environ. Toxicol. Chem. 18 (1999) 1779–1782.
[59] Y.H. Huang, T.C. Zhang, Kinetics of nitrate reduction by iron at near neutral pH, J. Environ. Eng. 128 (2002) 604–611.
[60] L. Zhang, W.A. Arnold, R.M. Hozalski, Kinetics of haloacetic acid reactions with Fe(0), Environ. Sci. Technol. 38 (2004) 6881–6889.
[61] H.-L. Lien, W.-X. Zhang, Nanoscale Pd/Fe bimetallic particles: catalytic effects of palladium on hydrodechlorination, Appl. Catal. B 77 (2007) 110–116.
[62] J.P. Fennelly, A.L. Roberts, Reaction of 1,1,1-trichloroethane with zero-valent metals and bimetallic reductants, Environ. Sci. Technol. 32 (1998) 1980–1988.
[63] W.-X. Zhang, C.-B. Wang, H.-L. Lien, Treatment of chlorinated organic contaminants with nanoscale bimetallic particles, Catal. Today 40 (1998) 387–395.
[64] D.M. Cwiertny, S.J. Bransfield, K.J.T. Livi, D.H. Fairbrother, A.L. Roberts, Exploring the influence of granular iron additives on 1,1,1-trichloroethane reduction, Environ. Sci. Technol. 40 (2006) 6837–6843.
[65] N.V. Myung, K. Nobe, Electrodeposited iron group thin-film alloys: structure–property relationships, J. Electrochem. Soc. 148 (2001) C136–C144.